THEORETICAL STUDY OF THE BONDING BETWEEN ALGINATE AND GRAPHENE OXIDE THROUGH THE INTERACTION OF ITS CARBOXYLIC GROUPS WITH THE DIVALENT METALS CU²⁺, CO²⁺, ZN²⁺, AND MN²⁺

CARLOS SOLOAGA ARDILES

Department of Chemistry, Faculty of Sciences, Universidad de Tarapacá, Avenida General Velásquez 1775, PO Box 7D, Arica-Chile.

ABSTRACT

The alginate-graphene oxide mixture has been extensively studied due to its capacity to adsorb heavy metals, presenting higher structural and thermal stability than alginate. These properties and adsorption capacity would be related to the presence of functional groups present in the hydrocarbon chain of alginate and graphene oxide, such as carboxylic, hydroxyl, ketone, and epoxy groups; in the present study, the interaction of transition cations in their divalent states Cu^{2+}, Co^{2+}, Zn^{2+} and Mn^{2+}, which act as bridges when interacting with carboxylic groups of alginate and graphene oxide, was studied. Theoretical calculations based on density functional theory (DFT) were used for this purpose. For this, the lowest energy geometries were determined at the B3LYP level of theory through the effective central potential (ECP) with LanL2DZ bases. The chemical nature of the interactions under study was determined using the natural bond orbitals (NBO) method, topological analysis of the electronic location function (ELF), and the quantum theory of atoms in molecules (QTAIM). The results showed that the interactions between the metals under study with the carboxylic groups of alginate and graphene oxide are of the coordinated type with a high electrostatic component, which varies according to the metal, where the binding strength and stability, according to the degree of electronic delocalization, was as follows; ALG-Cu-GO > ALG-Co-GO > ALG-Mn-GO > ALG-Zn-GO. These results correlate with the available information, concerning the adsorption capacity of the alginate-graphene oxide mixture, for those metallic species. Furthermore, this interaction could influence the type of structural morphology of the alginate-graphene oxide beads.

Keywords: Alginate-graphene oxide mixture; adsorption metals; DFT; NBO; ELF; QTAIM.

1. INTRODUCTION

Natural biopolymers present a wide range of physical and chemical properties, which have led to various applications in different fields, such as technology, medicine, environment, among many others (1). Alginate (Fig. 1) is a natural biopolymer obtained from brown algae by relatively inexpensive extraction methods (2). It has hydrophilic properties and good biocompatibility, which has allowed its wide use in medicine (3). Additionally, its ability to remove heavy metals in contaminated water has been studied with promising results (4). Its structure is composed of fragments of D-mannuronic acid (M) and L-guluronic acid (G), with M and G present in different proportions and alternations, depending on the origin of the alginic acid (such as brown algae or microorganisms). Several of their properties result from the presence of functional groups, such as carboxylic acids, hydroxyl groups, and ketone oxygens, attached to the hydrocarbon chain (5). However, their physical resistance and thermal stability are low, which limits their applications at the industrial level (6). In contrast, sodium alginate has good properties for forming high-density and low porosity hydrogels, which are essential in adsorption process (7). Gelation occurs when divalent cations such as Ca^{2+} interact with G-blocks to produce alginate gels with two bound G residues, which generate a cavity to which calcium atoms are bonded, giving rise to the well-known *egg-crate model* (8).
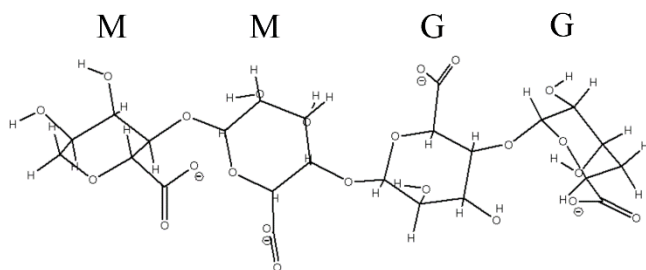

Figure 1. Structure of blocks G and M of alginate.

Studies on polymer blends have shown that materials with properties different from those of their constituents can be generated, expanding their uses and applications. For instance, the mixture of alginate with chitosan presents better physical properties and improves the adsorption performance of a series of heavy metals in contaminated waters (9; 10). Furthermore, it has been studied that combining inorganic materials, such as graphene oxide (GO), improves sodium alginate's structural and thermal stability (11-13). GO presents a large specific surface area, availability of randomly distributed functional groups (hydroxyl, carboxylic, epoxy), capable of interacting with metal ions, high porosity, and high mechanical strength (14). These chemical properties make it compatible with the properties of alginate, which allows the interaction between the two substances.

Graphene consists of a flat hexagonal lattice structure, one atom thick, where the carbon atoms present an sp^2 hybridization, where the unhybridized p orbital forms π bonds, thus the remaining valence electron is delocalized in a π system (15-17) (Fig. N2).
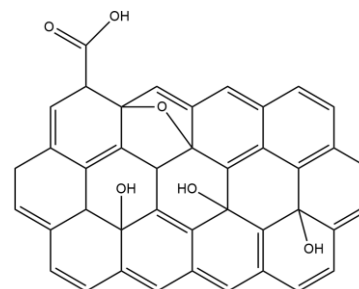

Figure 2. Schematic representation of graphene oxide structure

Several studies have shown that one of the determining factors in the physical properties of this mixture, such as its mechanical strength, porosity, and diffusion in water, is because divalent metal cations, such as Ca^{2+}, allow the entanglement of alginate with graphene oxide nano-layers to form sizeable cross-linked GO networks within calcium alginate hydrogels (4; 18; 19). Based on this information, in this work, we propose to study, through a theoretical approach, the analysis of the interaction between the divalent transition cations Cu^{2+}, Co^{2+}, Zn^{2+}, and Mn^{2+}, which would act as ligands by binding to the oxygen atoms of alginate carboxylic groups and terminal carboxylic groups of graphene oxide (ALG-M-GO), according to the model proposed in previous studies (18-20). For this purpose, different theoretical models, such as DFT, ELF, NBO, and QTAIM, will be used to analyze the chemical nature and stability of the bonds formed.

2. THEORETICAL CALCULATIONS

2.1. Model

As mentioned previously, our model is based on previous experimental studies, which propose the interaction of a divalent metal (M), acting as a bridge, interacting with the oxygens of the carboxylic groups present in both the alginate (21) and the graphene oxide (GO) (Figure 3).

The model consists of an alginate chain formed by two M-blocks linked to two G-blocks through a GM glycosidic bond. The torsion angle of each glycosidic bond in the molecule was modified to obtain the lowest energy structure.

Corresponding author email: csoloaga@academicos.uta.cl

Meanwhile, the graphene oxide model comprises 6 rings of 6 carbon atoms with alternating π bonds and randomly arranged hydroxyl, epoxy, and carboxylic groups. In the gas phase, each structure was optimized by density functional theory (DFT), with the B3LYP hybrid at the 6-31G (d, p) level of theory. The alginate chain interacted with the graphene oxide using different metals as a bridge (Figure 3). The distance and orientation of the GO and the different metals under study regarding the alginate chain were modified to obtain the lower energy structures. The optimization was carried out using effective central potential (ECP) with LanL2DZ bases for the structures where the different transition elements participate as bridges.
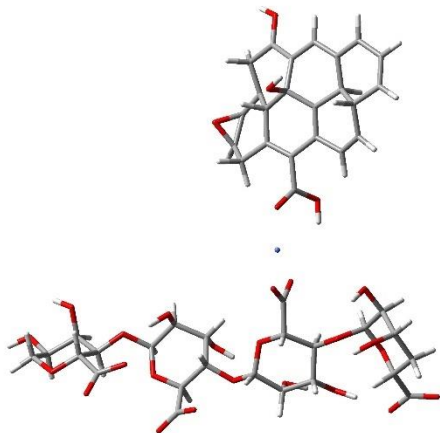
Figure 3. Representation of the model under study Alginate-Metal-Graphene Oxide (ALG-M-GO (M: Cu $^{2+}$, Co $^{2+}$, Zn $^{2+}$, Mn $^{2+}$))

3. COMPUTATIONAL METHOD

The geometry of the systems under study was optimized using G16 software. The NBO calculations were obtained using an internal module of G16. The calculations of the index, ELF, populations, variance, relative flux, link polarization, and visualization of the ELF diagrams, QTAIM analysis, and NBO visualization were performed using Multiwfn 3.8 software. Chiquera X 1.0 software was used to visualize the location of the attractors.

3.1. NATURAL BOND ORBITAL (NBO)

The Natural Bond Orbitals (NBO) method has been widely described in the literature (22) and applied to try to represent the chemical nature of the interactions between organic molecules with different metals (23). The NBO proposes the interaction between atoms based on the transfer of charge from a full orbital σ_i, called electron donor, to the valence of an anti-bonding orbital σ_j^*, defined as the electron acceptor, through a process known as charge transfer or of the donor-acceptor type. This method consists of transforming a wave function in the fundamental state into localized orbitals, which can be related to the chemical bond, according to Lewis. The energy associated with this charge transfer is obtained from the secondary perturbation theory, which relates the Fock operator ($\hat{F}$) to the energy of the natural bond orbitals ($\varepsilon_i = \langle \sigma_i | \hat{F} | \sigma_i \rangle$, $\varepsilon_{j^*} = \langle \sigma_j^* | \hat{F} | \sigma_j^* \rangle$), according to the following expression.

$$E_{i \to j}^{(2)} = -2 \frac{\langle \sigma_i | \hat{F} | \sigma_j^* \rangle}{\varepsilon_{j^*} - \varepsilon_i} \qquad (1)$$

The magnitude of the fe Fock matrix elements will be correlated with the symmetry of the bonding and anti-bonding orbitals in this study to represent the energetic stabilization according to the generalized principle of maximum overlap between bonds and anti-bonds (24).

3.2. Electron localization function (ELF)

The idea of the electronic localization function (ELF) involves dividing a molecular system into localization regions, representing the total number of electron pairs in that system. These regions correspond to the electron pair density, which gives the probability of finding an electron of a particular spin at a point in space when a second electron of opposite spin is at a certain distance (25). Savin et al. propose that the electron pair density can be generalized to any density independent of spin (26), according to the following equation.

$$D = \frac{1}{2} \sum_i (\nabla \phi_i)^2 - \frac{1}{8} \frac{(\nabla \rho)^2}{\rho} \qquad (2)$$

The ELF is a method for mapping the probability of electron pairs in multi-electron systems. It makes it possible to distinguish between the different electronic shells of atoms and molecules and identify bond types and lone pairs.

Through the function of the electronic localization feature, it is possible to divide the Euclidean space into basins of attractors (local maxima), in which the electron pairs are located. It is called the central basin (C), which surrounds a nucleus (except a proton); otherwise, it is called the valence basin (V). The latter will always be connected to at least one central basin. The latter is the case of a lone pair of electrons, whose attractor is called monosynaptic. In comparison, an attractor is called disynaptic when a basin is connected to two central basins, representing a covalent bond (27).

Chemical-relevant information can be obtained from the concepts mentioned earlier. For example, by integrating the electron density relative to the volume of the basin, it is possible to obtain its electron population (Eq. 2). Also, it is possible to know the electron pair flux (σ2) (Eq. 3), whose fluctuation can be associated with an interaction between atoms (27). For comparison between molecular systems where the chemical nature of an atom varies, the relative flux $\lambda(\bar{N}; \Omega_i)$ (Eq. 4) is applicable since the variance is an extensive property of the system (28). The model proposed by Raud and Jansen, based on the combination of the complementary topological partitions of the electron density, will also be used to determine the degree of polarity of the interactions under study. The equations for the properties above are presented below, respectively (29).

$$\bar{N}(\Omega_i) = \int_{\Omega_i} \sigma(r) dr = \bar{N}^\alpha(\Omega_i) + \bar{N}^\beta(\Omega_i) \qquad (3)$$

$$\sigma^2(\Omega_A) = \int_{\Omega_A} \int_{\Omega_A} \Gamma_{XC}(\vec{r}_1, \vec{r}_2) d\vec{r}_1 d\vec{r}_2 + \bar{N}(\Omega_A) = \bar{N}(\Omega_A) - \lambda(\Omega_A) \qquad (4)$$

$$\lambda_F(\Omega_A) = \frac{\sigma^2(\Omega_A)}{\bar{N}(\Omega_A)} \qquad (5)$$

1.3. QTAIM Analysis

Quantum Theory of Atoms in Molecules (QTAIM) offers another way to characterize chemical bonds through the topological analysis of the electronic density and its Laplacian function (30). This analysis, proposed by Bader, is based on the topology of the charge distribution, ρ, which is described by critical points PC ($\Delta \rho = 0$) (31). Four types of PCs with non-zero eigenvalues can be characterized; (3, -3), local maximum (attractor), (3, -1), first-order saddle point, (3, +3), second-order saddle point, and (3, +1), local minimum (source). From each critical tie point (CTP), a pair of gradient lines arise that culminate their path over the neighboring nuclei, defining a line along which it is maximal (32). Moreover, through this theory, there are a series of local properties in the PCE, which can characterize an interaction, such as; the Laplacian of the electron density, given by the equation N, which allows for to identify regions of charge concentration ($L_{r_b} > 0$) and charge depression ($L_{r_b} < 0$).

$$L_{r_b} = -\frac{1}{4} \nabla^2 \rho(r_b) \qquad (6)$$

Other local properties are the kinetic energy densities $G(r_b)$ (magnitude always positive), and the potential energy densities $V(r_b)$ (magnitude consistently negative), which according to the virial theorem, are related by equation 6.

$$2G(r_b) + V(r_b) = -L_{r_b} \qquad (7)$$

The exact quantities, however, can be related to the total electronic energy according to the following expression.

$$G(r_b) + V(r_b) = H(r_b) \qquad (8)$$

The joint analysis of these topological properties facilitates studying interactions between atoms. For example, the virial theorem tells us that a negative value of $H(r_b)$, where potential energy predominates over kinetic energy, can be interpreted as an accumulation of electron density in the PCE.

Consequently $|V(r_b)| > 2G(r_b)$ y $H(r_b) < 0$ are associated with shared layer interactions. Meanwhile, if $|V(r_b)| < 2G(r_b)$ y $H(r_b) > 0$, with closed-layer interactions (33). Another interesting property that allows characterizing types of interactions is the ratio between the absolute value of the power energy density concerning the kinetic energy density, according to the following expression.

$$|V(r_b)|/G(r_b) \qquad (9)$$

Where values of $|V(r_b)|/G(r_b) < 1$ indicate closed-layer interactions, while $|V(r_b)|/G(r_b) > 2$, covalent interactions are considered. When the values of this expression are between $1 < |V(r_b)|/G(r_b) < 2$, interactions of intermediate character are considered (29; 34).

4. RESULTS AND DISCUSSION

4.1. NBO Analysis

4.1.1. ALG-Cu-GO

Table 1 shows the NBO results for the ALG-Cu-GO system. The analysis shows that the (one-center) interactions occur by charge transfer from the O_{100} oxygens of the carboxylic acid of graphene and O_{76} and O_{77} of the carboxylic acid of alginate to the copper atom. According to the second-order hyperconjugative energy values, the most stabilizing interaction of the system occurs between the LP (2) (O_{76}) donor, whose low electronic population reveals a strong charge transfer to the LP* (6) (Cu) (acceptor) anti-bonding lone pair of the copper atom, with a value $E^{(2)}$ of 68.02 Kcal mol-1, with a distance of 1.87 A^0. Then, the charge transfer from LP (2) (O_{100}) (donor) to LP* (6) (Cu) (acceptor) has the second highest value of $E^{(2)}$ (39.68 Kcal mol-1), with a binding distance of 1.94 A^0. The interaction between O_{77} and Cu is also observed to be of minor relevance (2.74 A^0) since the $E^{(2)}$ values are low, where charge donation from LP (2) (O_{77}) to LP* (6) (Cu) would decrease the stability of the interactions involving LP* (6) (Cu), due to its high electronic occupancy (29; 35).

In Figure 4, the overlap of the natural bonding orbitals for the interactions between O76 (Fig. 4 A) and O_{100} with Cu (Fig. 4 B) is shown. For the charge transfer from LP (2) (O_{76}) and LP (2) (O_{100}) to LP* (6) (Cu), a decrease in the electron density of the donor (green-yellow (positive) and violet (negative) region) and an increase of this in the anti-bonding orbital of the acceptor (green (positive) and blue (negative) region) are seen, generating a broad interaction region around O_{76} and O_{100}, indicating a strong bond polarization (36; 37).
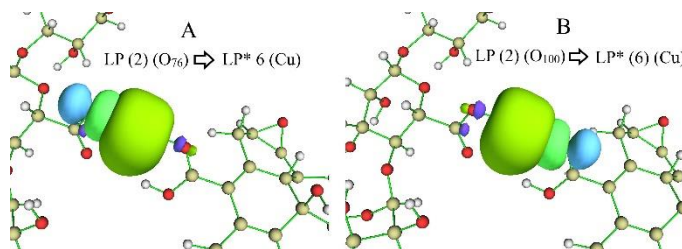
Figure 4. AB NBO orbitals for the most important interactions, in terms of $E^{(2)}$, in ALG-Cu-GO

Meanwhile, LP* 7 (O76) (Cu), with low occupancy, acts as a charge acceptor for both O_{76} and O_{100}, generating significant values of $E^{(2)}$, which indicates that the most relevant interactions in this system are between O_{100} (graphene), O_{76} (alginate), and copper. The energies obtained by second-order perturbation theory for charge transfers from occupied Lewis-type NBOs to empty non-Lewis-type NBOs indicate delocalization corrections concerning the idealized Lewis structure (38). The sum of the $E^{(2)}$ values for the charge transfer from O_{76} was 98.43 Kcal mol-1. In comparison, for O_{100}, it was 69.67 Kcal mol-1, which indicates that these interactions generate a high system stabilization by electronic delocalization in the bond region (23; 39).

Table 1. Significant interactions (greater than 2.00 Kcal mol-1) and their second-order perturbation energies $E^{(2)}$ in the ALG-Cu-GO system.

Donor (i)	Occupancy	Acceptor (j)	Occupancy	$E^{(2)}$ Kcal mol^{-1}
σ (C_{21}-O_{76})	1.99492	LP* *6* (Cu)	0.33404	2.60
σ (C_{21}-O_{76})		LP* *7* (Cu)	0.05351	2.21
LP *1* (O_{76})	1.99731	LP *2* (Cu)		11.46
LP *2* (O_{76})	1.75654	LP* *6* (Cu)	0.33404	68.02
LP *2* (O_{76})		LP *7* (Cu)	0.05351	9.37
LP *3* (O_{76})	1.68401	LP *9* (Cu)	0.02034	4.77
LP *2* (O_{77})	1.84213	LP* *6* (Cu)	0.33404	2.95
LP *2* (O_{77})		LP* *8* (Cu)	0.02833	2.79
LP *1* (O_{100})	1.93654	LP* *6* (Cu)	0.33404	8.64
LP *1* (O_{100})		LP* *7* (Cu)	0.05351	10.00
LP *1* (O_{100})		LP* *8* (Cu)	0.02833	2.36
LP *2* (O_{100})	1.93654	LP* *6* (Cu)	0.33404	39.68
LP *2* (O_{100})		LP* *7* (Cu)	0.05351	8.99

4.1.2 ALG-Co-GO

The NBO analysis for the ALG-Co-GO system shows that the interactions between the O_{100}, O_{76}, and O_{77} oxygens with the cobalt atom occur by charge transfer to the metal (one-center interaction). In Table 2, the hyperconjugative energy values are presented, where the charge transfer from LP (2) (O_{76}) to LP* (5) (Co) is the most important, with a bond distance of 1.91 A^0. They are followed by transfers from LP (2) (O_{77}) to LP* (6) (Co) (1.95 A0) and from LP (2) (O_{100}) to LP* (5) (Co) (1.96 A^0). The above is reflected in the low occupancy values of the lone pairs of oxygens, which act as donors (Table 2).

Figure 5 shows the NBO orbital interactions for these interactions. The overlap of the p_y orbital of O_{76} with the d_{yz} orbital of Co ($E^{(2)} = 64.23$ Kcal mol^{-1}) can be seen (Fig. 5 A). In Figure 5 B, the interaction between the p_y orbital of O77

and an s orbital of the metal is shown ($E^{(2)} = 44.98$ Kcal mol^{-1}), and in Figure 5 C, the overlap between the p_y orbital of O_{100} and the d_{yz} orbital of Co ($E^{(2)} = 26.66$ Kcal mol^{-1}). All of them decrease the electron density of the donor and increase the acceptor, suggesting the formation of oxygen-metal polarized bonds. Additionally, when considering the sum of the values of $E^{(2)}$, it can be seen that the oxygen-metal interactions generate a higher degree of electronic delocalization than in the ALG-Cu-GO system. The charge transfers from O_{76} to the metal generate a total hyperconjugative energy value of 133.66 Kcal mol-1. The charge transfers from O_{77} to Co generate a value of $E^{(2)}$ 95.29 Kcal mol-1, and the transfer from O_{100} to metal a value of 86.04 Kcal mol-1. In this system, the interaction between O77 and Co is important in stabilizing the system (24; 39).

Table 2. Significant interactions (greater than 2.00 Kcal mol-1) and their second order perturbation energies $E^{(2)}$ in the ALG-Co-GO system.

| Donor (i)	Occupancy	Acceptor (j)	Occupancy	$E^{(2)}$ Kcal mol^{-1}
σ (C$_{21}$-O$_{76}$)	1.99401	LP* 5 (Co)	0.38729	3.67
σ (C$_{21}$-O$_{76}$)		LP* 7 (Co)	0.06137	3.52
σ (C$_{21}$-O$_{77}$)	1.99611	LP 6 (Co)	0.23774	5.21
LP 1 (O$_{76}$)	1.95073	LP* 5 (Co)	0.38729	5.69
LP 1 (O$_{76}$)		LP 6 (Co)	0.23774	4.91
LP 1 (O$_{76}$)		LP 7 (Co)	0.06137	13.94
LP 2 (O$_{76}$)	1.71066	LP* 5 (Co)	0.38729	64.23
LP 2 (O$_{76}$)		LP* 6 (Co)	0.23774	22.70
LP 2 (O$_{76}$)		LP* 7 (Co)	0.06137	9.79
LP 1 (O$_{77}$)	1.95556	LP* 7 (Co)		11.14
LP 1 (O$_{77}$)		LP* 8 (Co)	0.03498	9.90
LP 2 (O$_{77}$)	1.68174	LP* 5 (Co)	0.38729	24.22
LP 2 (O$_{77}$)		LP* 6 (Co)	0.23774	44.98
LP 2 (O$_{77}$)		LP* 8 (Co)	0.03498	5.05
LP 1 (O$_{100}$)	1.92437	LP* 6 (Co)	0.23774	10.50
LP 1 (O$_{100}$)		LP* 7 (Co)	0.06137	10.15
LP 1 (O$_{100}$)		LP* 8 (Co)	0.03498	4.64
LP 2 (O$_{100}$)	1.80830	LP* 5 (Cu)	0.38729	26.66
LP 2 (O$_{100}$)		LP* 6 (Co)	0.23774	22.58
LP 2 (O$_{100}$)		LP* 7 (Co)	0.06137	8.51
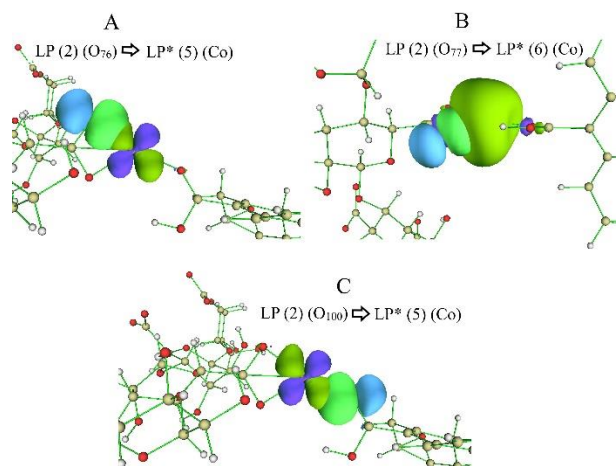
Figure 5. ABC NBO orbitals for the most important interactions, in terms of $E^{(2)}$, in ALG-Co-GO

4.1.3. ALG-Zn-GO

In the ALG-Zn-GO system, the most stabilizing interactions of the system are produced by charge transfers from the lone pairs of O$_{76}$, O$_{77}$ y O$_{100}$, which act as a donor, to the metal center, which acts as an acceptor. According to Table 3, the transfer from LP (2) (O O$_{76}$, O$_{77}$ y O$_{100}$,) to LP* 6 (Zn) generates the highest hyperconjugative energy value (42.28 Kcal mol^{-1}), with a binding distance of 1.98 A^0. Followed by charge transfer from LP (2) (O$_{77}$) to LP* (6) (Zn) (41.14 Kcal mol^{-1}) (2.01 A^0) and then by charge transfer from LP 2 (O$_{100}$) to LP* 6 (Zn) (33.65 Kcal mol^{-1}) (1.96 A^0). In Figure 6 ABC, the interactions of the NBO orbitals are shown for these interactions, respectively. The p$_y$ orbitals of O$_{76}$, O$_{77}$ and O$_{100}$, overlap with the 4S orbital of Zn (98.21 % *S* character). The latter has high occupancy, weakening the bonds in which LP* (6) (Zn) participates. Similarly to the previously analyzed systems, a decrease in the electron density of the donor and an increase in that of the acceptor is observed, suggesting the formation of polarized bonds. The sum of the values $E^{(2)}$ for charge transfer from LP (2) (O$_{76}$) to LP* (6) (Zn) was 75.06 Kcal mol^{-1}. 69.17 Kcal mol^{-1} for charge transfer from LP (2) (O$_{77}$) to LP* (6) (Zn) and the interaction LP (2) (O$_{100}$) to LP* (6) (Zn) a value of 85.65 Kcal mol^{-1}, indicating stabilization of the system by delocalization of the electron density, although to a lesser degree than observed in the previous systems.

Table 3. Significant interactions (greater than 2.00 Kcal mol^{-1}) and their $E^{(2)}$ second-order perturbation energies in the ALG-Zn-GO system.

	Occupancy	Acceptor (j)	Occupancy	$E^{(2)}$ Kcal mol^{-1}
π (C$_{21}$-O$_{77}$)	1.98438	LP* 9 (Zn)	0.03293	3.10
LP 1 (O$_{76}$)	1.96252	LP* 6 (Zn)	0.41045	2.86
LP 1 (O$_{76}$)		LP* 7 (Zn)	0.08234	9.01
LP 2 (O$_{76}$)	1.76346	LP* 6 (Zn)	0.41045	42.28
LP 2 (O$_{76}$)		LP* 7 (Zn)	0.08234	16.85
LP 3 (O$_{76}$)	1.65403	LP* 9 (Zn)	0.03293	4.07
LP 1 (O$_{77}$)	1.96252	LP* 6 (Zn)	0.41045	3.43
LP 1 (O$_{77}$)		LP* 8 (Zn)	0.05972	7.78
LP 2 (O$_{77}$)	1.78315	LP* 6 (Zn)	0.41045	41.14
LP 2 (O$_{77}$)		LP* 8 (Zn)	0.05972	12.57
LP 2 (O$_{77}$)		RY* 4 (Zn)	0.00089	4.07
LP 1 (O$_{100}$)	1.93314	LP 6 (Zn)	0.41045	6.77
LP 1 (O$_{100}$)		LP* 7 (Zn)	0.08234	4.38
LP 1 (O$_{100}$)		LP* 8 (Zn)	0.05972	11.66
LP 2 (O$_{100}$)	1.83327	LP* 6 (Zn)	0.41045	33.65
LP 2 (O$_{100}$)		LP* 7 (Zn)	0.08234	14.24
LP 2 (O$_{100}$)		LP* 8 (Zn)	0.05972	8.38
LP 2 (O$_{100}$)		RY* 4 (Zn)	0.00089	6.57
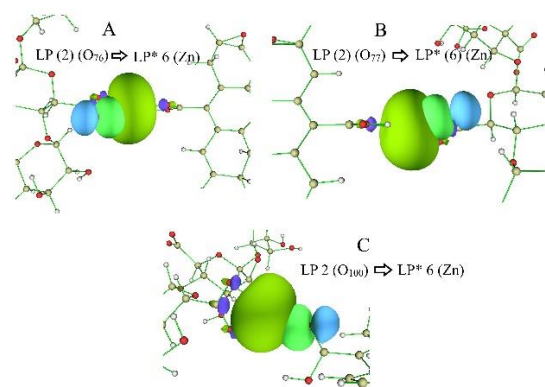
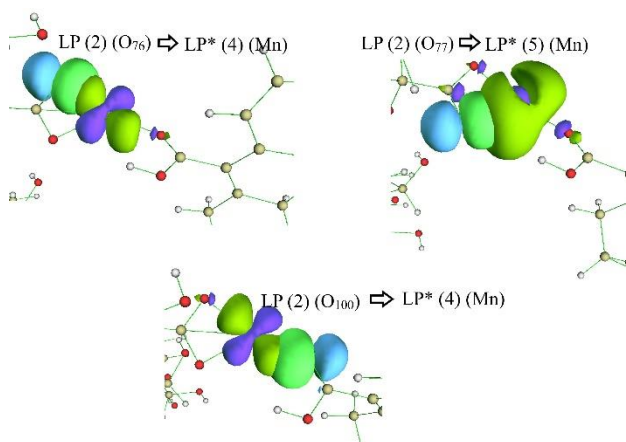**Figure 6.** ABC NBO orbitals for the most important interactions, in terms of $E^{(2)}$, in ALG-Zn-GO.

4.1.4. ALG-Mn-GO

In this system, the trend is maintained for interactions through charge transfer from the oxygen atoms under study to the metal, which is reflected in the low populations of LP (2) (O_{76}), LP (2) (O_{77}), and LP (2) (O_{100}) (38). Here, the interaction between the donor LP (2) (O_{76}) to the acceptor LP* (4) (Mn) generates high stabilization ($E^{(2)}$ = 63.38 Kcal mol-1), with a binding distance of 1.97 A⁰. Figure 7 A shows the overlap of the p_y orbital (91.78 % p character) of O_{76} with the d_{yz} orbital of Mn (92.96 % d character), where the decrease of the electron density of the donor and the increase of this in the acceptor suggests the formation of a polarized bond. Another important interaction is produced by charge transfer from LP (2) (O_{77}) (donor) to LP* (5) (Mn) (acceptor), with a high perturbative energy value ($E^{(2)}$ = 52.61 Kcal mol-1), (1.99 A⁰). In Figure 7 B, the overlap of the d_{yz} orbital (92.89 % p character) of O_{77} with the 4S orbital (69.10 % S character) of Mn results in a polarized bond due to the increase and decrease of the electron density of the acceptor and donor, respectively. An analogous situation is seen for the one-center interaction between LP (2) (O_{100}) and LP* (4) (Mn). In this, the p_y orbital of O_{100} overlaps with the d_{yz} orbital of Mn (Fig. 7 C), generating a high hyperconjugative energy value ($E^{(2)}$ = 32.28 Kcal mol-1) and a bond distance of 1.98 A⁰. The sum of the values for the mentioned interactions is the highest obtained for the systems under study. Thus, for the interaction between O_{76} and Mn, the total value of second-order perturbation energy was 100.21 Kcal mol-1. For the interaction between O_{77} and Mn, this value was 95.15 Kcal mol-1, while the interaction between O_{100} and p_y Mn $E^{(2)}$ was 87.25 Kcal mol-1. These results suggest a high structural stabilization by electronic delocalization.

Table 4. Significant interactions (larger than 2.00 Kcal mol-1) and their $E^{(2)}$ second-order perturbation energies in the ALG-Mn-GO system.

Donor (i)	Occupancy	Acceptor (j)	Occupancy	$E^{(2)}$ Kcal mol-1
σ (C_{21}-O_{77})	1.99542	LP* *5* (Mn)	0.22417	5.93
	1.95330	LP* *5* (Mn)		2.63
LP *1* (O_{76})		LP* *6* (Mn)	0.05950	11.82
LP *2* (O_{76})	1.75030	LP* *4* (Mn)	0.31244	63.38
LP *2* (O_{76})		LP* *5* (Mn)	0.22417	13.65
LP *2* (O_{76})		LP* *6* (Mn)	0.05950	8.94
LP *3* (O_{76})	1.61017	LP* *9* (Mn)	0.01370	2.42
LP *1* (O_{77})	1.95560	LP* *5* (Mn)	0.22417	11.15
LP *1* (O_{77})		LP* *7* (Mn)	0.03473	7.86
LP *2* (O_{77})	1.72326	LP* *4* (Mn)	0.31244	14.56
LP *2* (O_{77})		LP* *5* (Mn)	0.22417	52.61
LP *2* (O_{77})		LP* *7* (Mn)	0.03473	4.01
LP *3* (O_{77})	1.63554	LP* *8* (Mn)	0.02558	4.96
LP *1* (O_{100})	1.92330	LP* *4* (Mn)	0.31244	5.80
LP *1* (O_{100})		LP* *5* (Mn)	0.22417	10.38
LP *1* (O_{100})		LP* *6* (Mn)	0.05950	9.48
LP *1* (O_{100})		LP* *7* (Mn)	0.03473	3.62
LP *2* (O_{100})	1.81350	LP* *4* (Mn)	0.31244	32.38
LP *2* (O_{100})		LP* *5* (Mn)	0.22417	18.55
LP *2* (O_{100})		LP* *6* (Mn)	0.05950	7.04
LP *3* (Mn)	1.58583	π* (C_{99}-O_{100})	0.32717	6.79

Figure 7. ABC NBO orbitals for the most important interactions, in terms of $E^{(2)}$, in ALG-Mn-GO

4.2. Electronic Localization Function Analysis (ELF)

4.2.1. ALG-Cu-GO

The electronic localization function was used further to investigate the chemical nature of the studied interactions. Figure 8 shows the ELF diagram for the interaction between O_{76}, O_{77}, and O_{100} with the copper atom. The degree of electronic localization, determined by this function, varies between 0 and 1.00, where the red color represents the regions of high localization in these diagrams (values higher than 0.8) (40). High delocalization of the core electrons in the metal (average ELF values, represented by the orange, green and blue colors) and a distortion of the valence shell, a product of the interaction with the oxygens, can be seen in the image, which could suggest some degree of covalence in the formation of these bonds (27; 41-43). Conversely, the non-bonding lone pair of O_{76}, which is oriented to the metal, shows increased delocalization (orange color) and distortion of the electron density.

Meanwhile, it can be seen that the degree of delocalization of the O_{100} lone pairs is lower (more intense orange color). The above is related to the NBO results, where the most robust oxygen-metal interaction is between O_{76} and Cu. The high hyperconjugative energy values indicated a high degree of electron

density delocalization. In this case, it can be related to the electron density found around the bonding region (blue color) with ELF values close to 0.5 (fermi gas reference value), which indicates 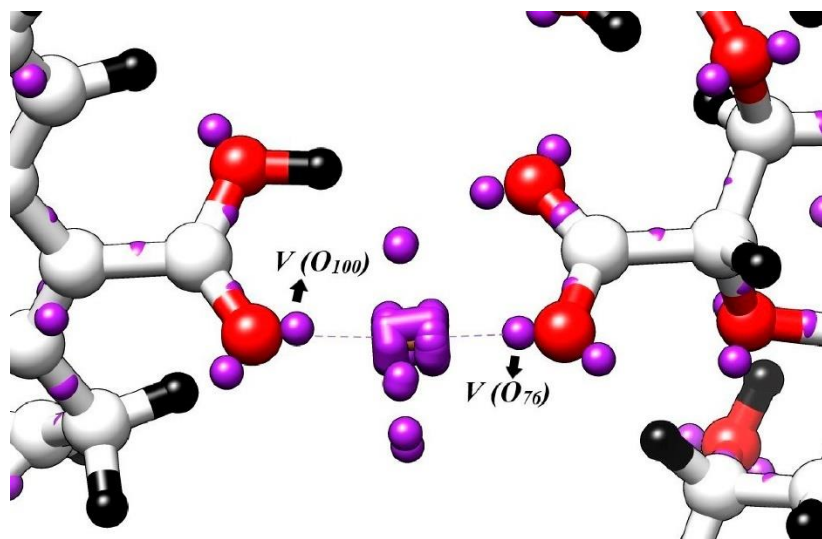a high degree of electronic delocalization (28; 44). In the case of O_{77}, its non-bonding pairs are seen to be more localized and homogeneously distributed, indicating little interaction with the metal (43) These results are also related to the low values of $E^{(2)}$, obtained in the analysis of natural bonding orbitals.
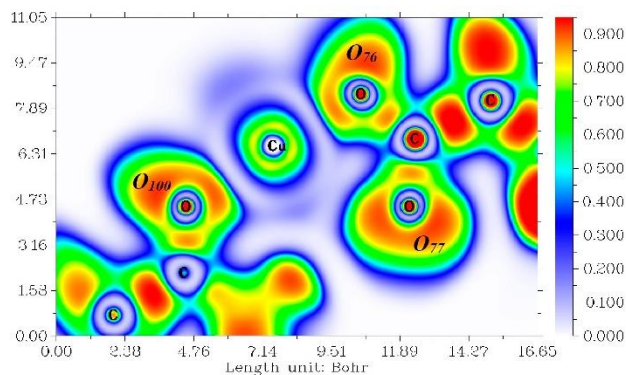
Figure 8. ELF diagrams for interaction O_{100}-Cu-O_{76}, in ALG-Cu-GO

The attractor analysis shows that the interactions between O_{76} and O_{100} with copper are the most important. According to the interpretation of Savin et al., the location of these may indicate the degree of covalence of the bond (28). Figure 9 shows that V (O_{76}) and V (O_{100}) are located directly on the metal bond line, suggesting some degree of covalence. Meanwhile, V (O_{77}) is not oriented toward the metal, which agrees with the ELF diagrams because no significant interaction

between O_{77} and Cu is seen. Furthermore, the integration of the electron density of the attractor basin shows a considerable decrease in the population of the core electrons of the copper atom (13.01e), well below the traditional value of 29 (Table 5).

Consequently, this indicates electron donation from the inner shells of the metal to the 3d valence region (45; 46). Moreover, V (O_{76}) presents a low population compared with oxygens attractors of the exact chemical nature present in the system, suggesting electron density donation to the metal, which according to Silvi & Savin, would be indicative of the formation of a dative bond. Meanwhile, the total population of the attractors of the lone pairs of O_{76} was 5.82e, while the overall average was 5.27e, indicating electronic donation and back-donation processes between O_{76} and Cu (47). The high population of V' (O_{76}) indicates redistribution of electron density donated from the metal aiming to decrease charge repulsion (48; 49). V' (O_{100}) presents a high population if the same comparison is made. It is suggested by the charge transfer from copper, which is also reflected in the total population of the attractors of both lone pairs, which was 5.48e, compared to the average reference value of 5.29e. The variance values are high for V (O_{76}), indicating a high electronic flux, which is confirmed by the value of the relative flux, which is very high, indicating an important degree of covalence in this interaction (50). A similar situation, although to a lesser degree, is seen in V (O_{100}), increases in both σ^2 and $\lambda_{(\bar{N};\Omega_i)}$), suggesting that in this interaction there is a certain degree of covalence in the bonding.

In contrast, the same magnitude values in V (O_{77}) show a trend very similar to the reference values, indicating that the interaction between O_{77} and Cu is weak. The analysis of the contributions shows that V (O_{76}) contributes 93.10 % to the population of that attractor, while V (O_{100}) contributes 96.25 %. These results suggest the formation of bonds with a certain degree of covalence, highly polarized. According to several authors, this agrees with the interpretation of an $O \rightarrow Cu$ dative bond (51).

Figure 9. Attractor populations of the lone pairs of O_{100}, O_{76}, O_{77} and valence and core attractors of copper, in ALG-Cu-GO.

Table 5. Populations (N), variance (σ^2,),), and relative flux ($\lambda_{(\bar{N};\Omega_i)}$), for attractors of O_{76}, O_{77} and O_{100} and average populations $\overline{(N)}$, , variance ($\bar{\sigma}^2$), and relative flux ($\bar{\lambda}_{(\bar{N};\Omega_i)}$) of reference attractors (oxygens (-OH, -COO-)), present in ALG-Cu-GO.

Attractor ALG-Cu-GO	Populations N/$\overline{N}$			Variance $\sigma^2/\overline{\sigma^2}$			Relative flow $\lambda_{(\bar{N};\Omega_i)}/\bar{\lambda}_{(\bar{N};\Omega_i)}$		
	-OH V(O_{76})	-CO V(O_{77})	-CO V(O_{100})	-OH V(O_{76})	-CO V(O_{77})	-CO V(O_{100})	-OH V(O_{76})	-CO V(O_{77})	-CO V(O_{100})
V (O)	2.03	2.53	2.4	1.14	1.19	1.23	0.59	0.47	0.51
V´(O)	3.79	2.95	3.09	0.33	1.27	0.66	0.09	0.16	0.21
V (O)	2.37	2.34		1.23	1.15		0.51	0.49	
V (O)	2.90	2.95		1.29	1.29		0.44	0.44	

4.2.2. ALG-Co-GO

Figure 10 shows the ELF diagram for the ALG-Co-GO system. In this diagram, the non-bonding pairs of O_{76} and O_{77} oriented to the metal show higher delocalization than the lone pair of O_{100}. Additionally, the electron density of the non-bonding pairs of the three oxygens shows an inhomogeneous distribution due to the interaction with the metal (48). Electrons in the core of the cobalt atom are highly delocalized (white color), and the valence shell is distorted, showing a significant difference with the spherical symmetry of the isolated atom, suggesting a strong interaction with the oxygen atoms (25; 42; 52). Also, a blue-colored region is seen in the interaction zones, similar to that observed in the system with copper. The ELF value is approximately 0.5, close to the Fermi gas reference value, indicating a delocalized electron density in the bonding region. These values agree with the hyperconjugative energy values, which indicate that such interactions generated a high charge delocalization.
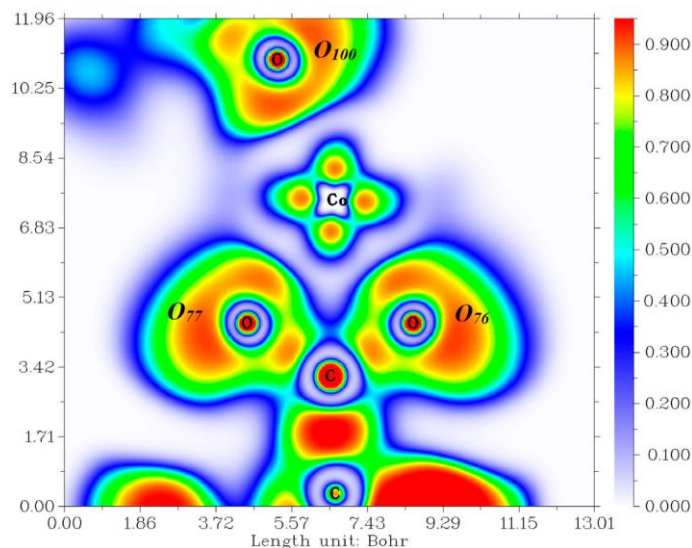

Figure 10. ELF diagrams for O_{100}-Co-(O_{76}, O_{77}) interaction in ALG-Co-GO.

The analysis of attractors, their populations, variance, and relative flux, shows that V (O_{76}) and V (O_{77}) are oriented towards the metal and located in the bond line with the metal (Figure 11); as already mentioned, this suggests a certain degree of covalence in the bond. In addition, the low populations of these attractors (Table 6), compared to the average reference values of oxygens of the same chemical nature, would indicate electron density donation to the metal, as this could be interpreted as the formation of a covalent bond (Figure 11). In addition, the low populations of these attractors (Table 6), compared to the

average reference values of oxygens of the same chemical nature, would indicate electron density donation to the metal, which could be interpreted as the formation of dative bonds (53). Therefore, this is related to the variance values and relative flux. The variance of these attractors is high, considering their low populations, which is reflected in the high relative flux, indicating a high delocalization of the electron density in the bond region (54).

Moreover, V (O_{100}) presents a higher population than the reference average, indicating charge transfer from the metal (55), which would increase the variance value. The relative flux, although with a value very similar to the reference, is still high, indicating that the electron density is delocalized close to the binding region, considering the location of V (O_{100}), which suggests a type of interaction with a certain covalent nature. The cobalt core population was 26.02e, slightly below the expected value of 27e. The analysis of the contributions showed that O_{76} contributes 95.00 % to the population of V (O_{76}), while the contribution of O_{77} to O_{100} was 95.00 %. The contribution from O_{77} to V (O_{77}) was 95.53 % and from O_{100} to V (O_{100}) was 97.52 %. These results agree with the interpretation of electrostatic interaction with some covalent degree between O_{100} and Co and that the dative bonds between O_{76} and O_{77} with Co are strongly polarized (56). The high values of electronic delocalization given by the relative flux are related to the second-order hyperconjugative energy values obtained in the NBO analysis. A mesomeric effect could occur between the atoms involved in such interactions (57).
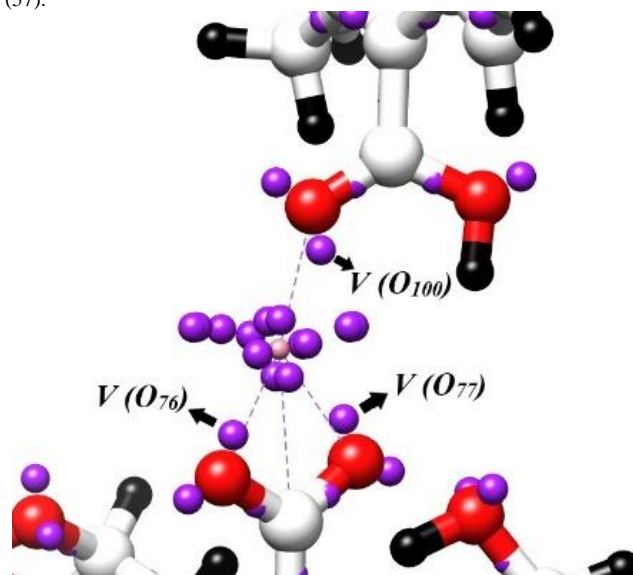
Figure 11. Attractor populations of the lone pairs of O_{100}, O_{76}, O_{77} and cobalt core and valence attractors in ALG-Co-GO.

Table 6. Populations (N), variance (σ^2), and relative flux ($\lambda_{(\bar{N};\Omega_i)}$), for O_{76}, O_{77} and O_{100} attractors and average populations ($\bar{N}$)), variance ($\bar{\sigma}^2$),), and relative flux ($\bar{\lambda}_{(\bar{N};\Omega_i)}$) of reference attractors (oxygens (-OH, -COO-)), present in ALG-Co-GO.

Attractor ALG-Co-GO	Populations N/$\bar{N}$			Variance $\sigma^2/\bar{\sigma}^2$			Relative flow $\lambda_{(\bar{N};\Omega_i)}/\bar{\lambda}_{(\bar{N};\Omega_i)}$		
	-OH $V(O_{76})$	*-CO* $V(O_{77})$	*-CO* $V(O_{100})$	*-OH* $V(O_{76})$	*-CO* $V(O_{77})$	*-CO* $V(O_{100})$	*-OH* $V(O_{76})$	*-CO* $V(O_{77})$	*-CO* $V(O_{100})$
V (O)	2.00	1,79	2,42	1.12	1.04	1.22	0.56	0.58	0.50
V′(O)	3,63	3,84	3,08	1.41	1.46	1.32	0.39	0.38	0.43
V (O)	2.42	2.25		1.23	1.14		0.50	0.51	
V (O)	3.00	3.11		1.30	1.3		0.43	0.42	

4.2.3. ALG-Zn-GO

Figure 12 shows the ELF diagram for the ALG-Zn-GO system. It highlights the high delocalization suffered by the electrons of the core and the valence layer of the metal, resulting from the interaction with the oxygen atoms under study. The same delocalized electron density around the bond region (ELF ≈ 0.5), as seen in the previous systems, is also appreciated. The lone pairs of O_{76} and O_{77} are highly delocalized and with an asymmetric electron density distribution, which reaffirms the idea of strong interactions. Meanwhile, the lone pair of O_{100} shows less delocalization and a more homogeneous distribution of the electron density of both lone pairs.
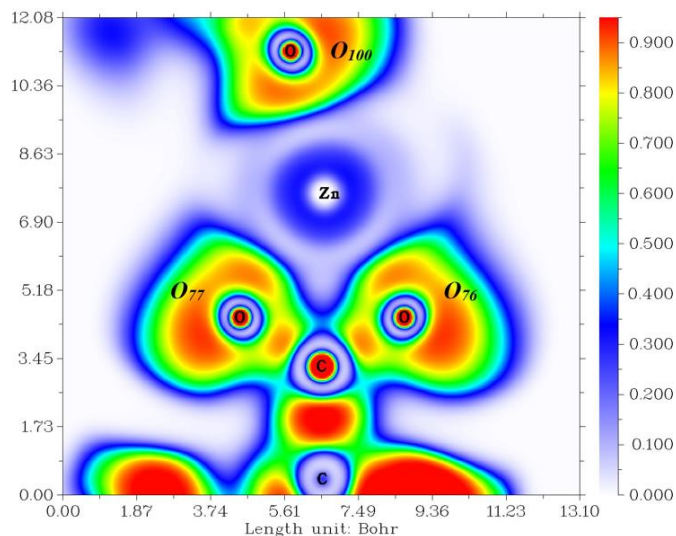
Figure 12. ELF diagrams for the O_{100}-Zn-(O_{76}, O_{77}) on ALG-Zn-GO

The analysis of the attractors and their location shows that V (O_{76}) and V (O_{77}) are oriented and located on the bond line (Figure 13), both with populations lower than the average reference values, indicating charge transfer to Zn (Table 7). Therefore, the above suggests dative bond formation, as already mentioned. The sum of the attractors of both lone pairs of O_{76} was 5.81e, while that of the reference lone pairs was 5.56e, indicating that charge transfer from the metal to O_{76} also occurs. Meanwhile, the same analysis for O_{77} showed that the total population for the lone pairs of this atom was 5.77e, while the sum of the

reference attractors was 5.36e, indicating charge transfer from the metal to this atom.

These results show electron density donating and back-donating processes between the mentioned elements. The analysis of the contributions showed that for the population of V (O_{76}), O_{76} contributed 90.73 %, while for V (O_{77}), O_{77} contributed 93.00 % to the attractor population. From this, it can be seen that the bonds formed are polarized. The idea of the degree of covalence of these interactions is supported by the values of variance and relative flux for both attractors. The variance values are high if we consider their populations, i.e., the electron flux increases as a result of the formation of the bonds. Likewise, the high value of the relative flux and considering the location of both attractors and the high electronic delocalization, is found in the bonding region.

Meanwhile, V (O_{100}) is close to the metal bond line, and its population is higher than the reference average, indicating charge transfer from the metal. Furthermore, its variance is higher than the reference values. The relative flux shows a trend similar to the reference values; however, it is a high value, which suggests that there is delocalized electron density in the bonding region, so it could be a type of interaction with a certain degree of covalence where the electrostatic component is important between O_{100} and Zn. The above is confirmed by the value of the contribution to V (O_{100}), which was 95.08 % of its population.

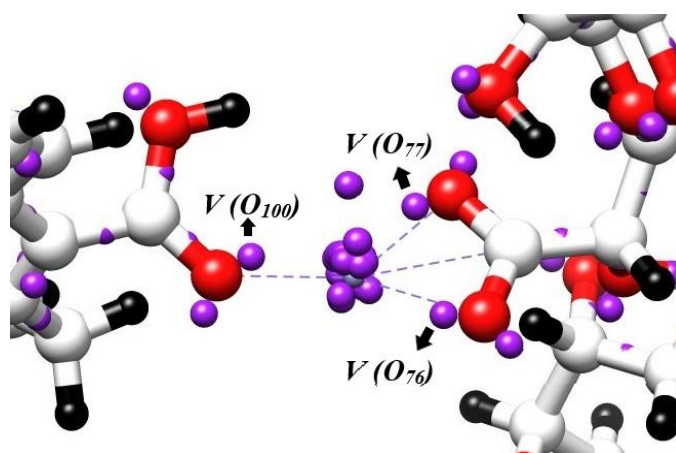**Figure 13.** Attractor populations of the lone pairs of O_{100}, O_{76}, O_{77} and valence and core attractors of zinc, in ALG-Zn-GO.

Table 7. Populations (N), variance (σ^2), and relative flux $\lambda_{(\bar{N};\Omega_i)}$), for attractors of O_{76}, O_{77}, and O_{100} and average populations ($\bar{N}$),), variance ($\sigma^\wedge 2$), and relative flux ($\lambda_{(\bar{N};\Omega_i)}$)of reference attractors (oxygens (-OH, -COO⁻)), present in ALG-Zn-GO.

Attractor ALG-Zn-GO	Populations N/$\bar{N}$			Variance $\sigma^2/\overline{\sigma^2}$			Relative flow $\lambda_{(\bar{N};\Omega_i)}/\bar{\lambda}_{(N;\Omega_i)}$		
	-OH V(O_{76})	-CO V(O_{77})	-CO V(O_{100})	-OH V(O_{76})	-CO V(O_{77})	-CO V(O_{100})	-OH V(O_{76})	-CO V(O_{77})	-CO V(O_{100})
V (O)	2,05	2,14	2,44	1.11	1.14	1.23	0.54	0.53	0.50
V´(O)	3,76	3,63	3,3	1.42	1.40	1.37	0.37	0.39	0.42
V (O)	2.45	2.25		1.20	1.15		0.49	0.51	
V (O)	3.11	3.11		1.31	1.32		0.42	0.42	

4.2.4. ALG-Mn-GO

Figure 14 shows the ELF diagram for the ALG-Mn-GO system. It shows a strong delocalization of the electrons of the metal core (white color) and a distortion of the valence layer, which would be a product of the interaction with the oxygens. The non-lone pairs of O_{76} and O_{77} are oriented to the metal and show

high delocalization and inhomogeneous electron density distribution. Meanwhile, the lone pair of O_{100} is oriented to the metal, showing less delocalization, and the electron density distribution of its lone pairs is more homogeneous. The same trend is observed concerning the electron density with values close to 0.5 ELF, indicating a high delocalization, as already mentioned.
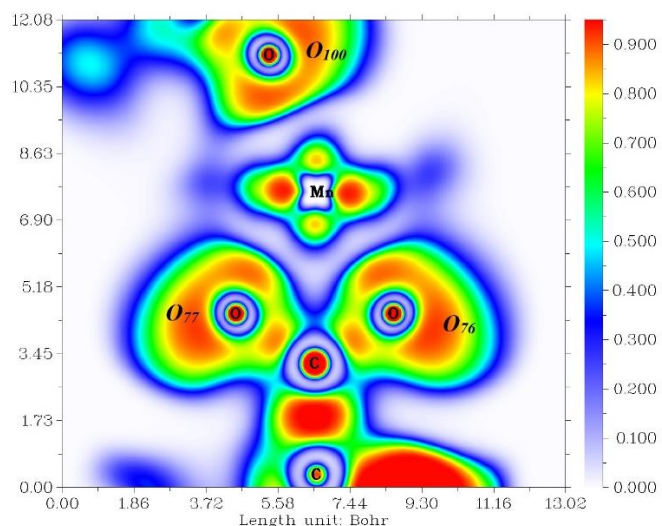
Figure 14. ELF diagrams for interaction O_{100}-Mn-(O_{76}, O_{77}) in ALG-Mn-GO

Figure 15 shows the monosynaptic attractors of the non-bonding pairs of the three oxygens under study. V (O_{76}) and V (O_{77}) are located directly on the binding line. According to Savin et al., this would suggest a certain degree of covalence in these interactions. According to the population values (Table 8), V (O_{76}) and V (O_{77}) present values below the reference average, which indicates charge donation to the metal. The sum of the population of both lone pairs of V (O_{76}) and V' (O_{76}) was 5.62e, while the average reference value was 5.50e. The same situation is seen for V (O_{77}) and V' (O_{77}) with a total population value (lone pairs) of 5.62e, concerning the reference value of 5.29e. The above indicates electron density donation and back-donation processes between these oxygen atoms and Mn. The localization and this exchange of electronic density would be an indication of a certain degree of covalence in these interactions. V (O_{100}), oriented towards the metal, is located close to the bond line. It has a higher than the average population, indicating charge transfer from the metal. The total

population of both monosynaptic attractors was 5.49e, while the reference average, as already mentioned, was 5.29e, so the main process in the formation of this bond is due to charge donation from the metal to O_{100}. The variance values for O_{76} and O_{77} are high if we consider their populations, indicating a high degree of electronic delocalization. These values are confirmed by the sharp increase in the relative flux, which indicates that there is an excess of delocalized electron density in the binding region (V (O_{76}) and V (O_{77}), (they are located in the metal-binding line). The increase in the relative flux of V (O_{100}) occurs to a lesser extent; however, it is high, and if we consider its localization, we can suggest a certain degree of covalence in the bond, where the electrostatic character would predominate. The contribution to the population of V (O_{76}) was 97.02%; for V (O_{77}), it was 96.96 %, while for V (O_{100}), it was 97.68 %. These values show that the polar component in these interactions is important.
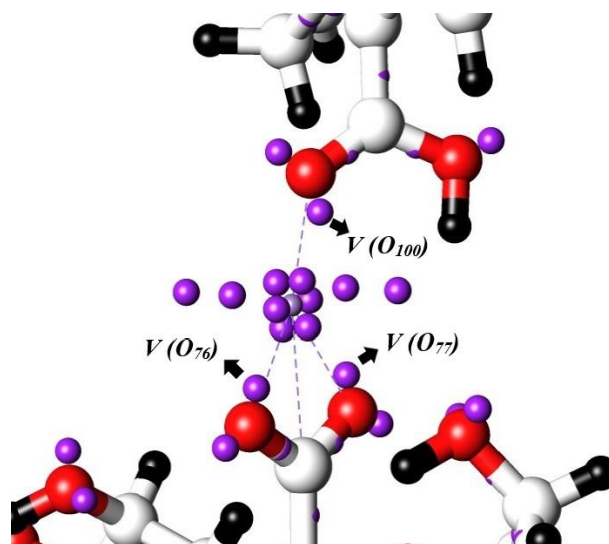
Figure 15. Attractor populations of the lone pairs of O_{100}, O_{76}, O_{77} and manganese core and valence attractors in ALG-Mn-GO.

Table 8. Populations (N), variance (σ^2),), and relative flux ($\lambda_{(\overline{N};\Omega_i)}$), for O_{76}, O_{77} and O_{100} attractors and average populations ($\overline{N}$), variance ($\overline{\sigma}^2$),), and relative flux ($\lambda_{(\overline{N};\Omega_i)}$ of reference attractors (oxygens (-OH, -COO$^-$)), present in ALG-Mn-GO.

Attractor ALG-Mn-GO	Populations $N/\overline{N}$			Variance $\sigma^2/\overline{\sigma}^2$			Relative flow $\lambda_{(\overline{N};\Omega_i)}/\overline{\lambda}_{(\overline{N};\Omega_i)}$		
	-OH $V(O_{76})$	-CO $V(O_{77})$	-CO $V(O_{100})$	-OH $V(O_{76})$	-CO $V(O_{77})$	-CO $V(O_{100})$	-OH $V(O_{76})$	-CO $V(O_{77})$	-CO $V(O_{100})$
V (O)	2,22	2,06	2,44	1.17	1.13	1.23	0.55	0.55	0.50
V´(O)	3,4	3,56	3,05	1.36	1.40	1.31	0.40	0.37	0.43
V (O)	2.69	2.42		1.25	1.19		0.46	0.49	
V (O)	2.81	2.87		1.27	1.27		0.45	0.44	

4.3. QTAIM Analysis

4.3.1. ALG-Cu-GO

Figure 16 shows the contour map of the Laplacian operator of the ALG-Cu-GO system. The dashed red lines represent charge depression, while the continuous blue lines represent charge concentration (58). In the latter, charge depression and polarization of the valence layer of the copper atom in the direction of the oxygen atoms can be seen. Likewise, the charge concentration in the metal tends to lose its spherical symmetry. Also, some polarization and charge leakage is observed from O_{76} towards the critical point of bonding with the metal. In contrast, in O_{100}, no charge leakage is observed towards the BCP, and its charge distribution is less affected in terms of symmetry by the interaction.

Figure 16. Contour map of $\nabla^2\rho$ of ALG-Cu-GO. The solid and dashed lines correspond to the negative regions and positive regions of $\nabla^2\rho$, respectively. Blue dots correspond to critical binding points.

Table 9 shows the values of $\nabla^2\rho_{BCP}$ for the O_{76}-Cu and O_{100}-Cu interactions. The results show positive values for this magnitude. Bader's interpretation of those results indicates that it corresponds to closed-layer interactions (electrostatic, Van de Waals interactions, coordinated bonds, hydrogen bridges) (59). The value for $\nabla^2\rho_{BCP}$ for O_{76}-Cu, is higher, indicating that this interaction is more intense (58). The above is confirmed by the values of electronic charge density ρ_{BCP}, which is considered a measure of bond strength (60). These values are relatively high if we contrast them with weak interactions, such as hydrogen bonds and halogen bonds ($\rho_{BCP} \approx 0,03$ a.u.) (61). Altogether, the above agrees with the ELF and NBO analyses, where the strongest interaction is that of O_{76}-Cu. Moreover, the negative values of the L_{r_b} function and positive value of H_{r_b} for the O_{100}-Cu interaction confirm that this bond is a closed-layer (polarized dative bond) (62). Furthermore, $H_{r_b} < 0$ for O_{76}-Cu. According to previous studies, it has been shown that with negative values of both magnitudes ($L_{(r_b)}$ and $H_{(r_b)}$) the decrease of $H_{(r_b)}$ together with the increase of the electronic charge density (ρ_{BCP}) in the BCP, is an indicator of the stabilization of the interaction due to the increase of the electrostatic component of the interaction (63). In Table 9, it can be seen that this magnitude follows this trend concerning ρ_{BCP}. These results are consistent with the ELF results, which showed that this interaction presents strongly polarized dative bonding characteristics. As already mentioned, the magnitude interval $1 < |V(r_b)|/G(r_b) < 2$ would allow us to discriminate the nature of both bonds. Accordingly, the O_{100}-Cu bond, being slightly less than 1, would be electrostatic, while the O_{76}-Cu bond, being greater than 1, would correspond to an intermediate nature between electrostatic and coordinated covalent bonding (64). However, the high electronic delocalization revealed by the NBO and ELF results could be related to the electronic resonance phenomenon, which would stabilize the system (65).

Table 9. Local topological properties at critical junction points in the ALG-Cu-GO system.

ALG-Cu-GO	O_{100}-Cu	O_{76}-Cu
$\nabla^2\rho_{BCP}$ (a.u.)	0,6038	0,7150
ρ_{BCP} (a.u.)	0,077	0,1023
$G(r_b)$ (a.u.)	0,1457	0,1883
$V(r_b)$ (a.u.)	-0,1404	-0,1979
L_{r_b} (a.u.)	-0,1509	-0,1788
$H(r_b)$ (a.u.)	0,0053	-0,0096
$|V(r_b)|/G(r_b)$	0,9637	1,0508

4.3.2. ALG-Co-GO

Figure 17 shows the Laplacian operator diagram of the electron density of the ALG-Co-GO system. The BCPs (3, -1), corresponding to the oxygen-metal bonds, are observed in this diagram. A strong polarization of the valence layer and charge leakage from the cobalt atom, directed towards the oxygen atoms, can be seen. Likewise, the valence layer of the O_{76} and O_{77} atoms is polarized and presents charge leakage towards the metal. Meanwhile, O_{100} presents a spherical symmetry without charge depression of its valence layer. This picture shows that the most robust interactions occur between O_{76}, O_{77}, and Co, which agrees with the ELF and NBO models.

Table 10 shows the results of the local properties of the BCPs for this system. The values of the electronic charge density indicate that the O_{76}-Co interaction is considered the strongest, followed in a smaller order of magnitude by that generated between O_{77}-Co and then by O_{100}-Co. The values of the Laplacian operator are high and positive, suggesting closed-layer type interactions. These values correlate with the balance between the kinetic energy density and the potential energy density given by the factor $L_{(r_b)}$, which are all less than zero. Since for O_{100}-Co, the value of $H_{(r_b)} > 0$, it reaffirms the closed-layer interaction character. Moreover, the values of $H_{(r_b)}$ for O_{76}-Co and O_{77}-Co are negative. The above would have an analogous explanation to what was observed in the previous system, i.e., the opposite trend between the values of $H_{(r_b)}$ and ρ_{BCP} would indicate that the electrostatic component would be necessary for the stabilization of these interactions.

While considering that the value of the ratio between the absolute value of the potential energy density concerning the kinetic energy density is more significant than one, it can be inferred that such interactions agree with a description of polar coordinating nature. At the same time, O_{100}-Co is slightly less than 1, which would imply an electrostatic character of this bond. However, the NBO and ELF results suggest that the electronic resonance effect is important due to the high electronic delocalization, so assigning a localized charge on O_{100} would not be the most accurate due to an electronic resonance effect (66).
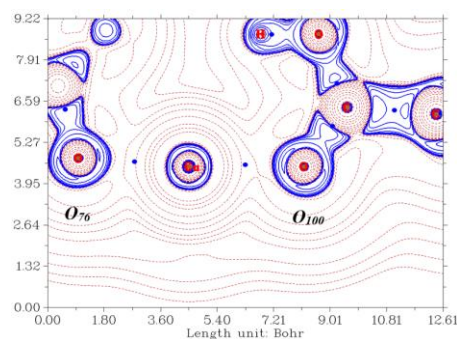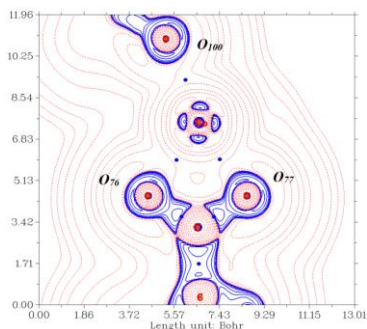

Figure 17. Contour map of $\nabla^2\rho$ of ALG-Co-GO. The solid and dashed lines correspond to the negative regions and positive regions of $\nabla^2\rho$, respectively. Blue dots correspond to critical binding points.

Table 10. Local topological properties at critical junction points in the system ALG-Co-GO.

ALG-Co-GO	O_{100}-Co	O_{76}-Co	O_{77}-Co
$\nabla^2\rho_{BCP}$ (a.u.)	0,5389	0,5745	0,5154
ρ_{BCP} (a.u.)	0,0750	0,9181	0,0850
$G(r_b)$ (a.u.)	0,1330	0,1561	0,1356
$V(r_b)$ (a.u.)	-0,1314	-0,1686	-0,1424
L_{r_b} (a.u.)	-0,1347	-0,1436	-0,1289
$H(r_b)$ (a.u.)	0,0017	-0,0125	-0,0068
$|V(r_b)|/G(r_b)$	0.9880	1.0800	1.0501

4.3.3. ALG-Zn-GO

Figure 18 shows the Laplacian operator diagram of the electron density of the ALG-Zn-GO system. In this, it can be seen that a strong charge leakage from the Zn valence layer in the direction of the oxygen atoms. O_{76} and O_{77} show a slight charge leakage in the direction of the metal. While in the lone pairs of both oxygens, the charge concentration is distorted. Meanwhile, the different layers in O_{100} remain almost unchanged. All three BCPs are charge leakage, and the value of $\nabla^2 \rho_{BCP}$ for those critical points is positive (Table 11). The charge density values are similar for all three BCPs and are slightly the lowest of the systems under study, particularly for the O_{76}-metal interaction. As mentioned above, a positive value of $\nabla^2 \rho_{BCP}$ indicates closed-layer interactions. In this system, the values of $L_{(r_b)}$ and $H_{(r_b)}$ are less than zero, so the opposite trend between $H_{(r_b)}$ and ρ_{BCP}, suggest that the system would tend to be stabilized mainly by the electrostatic component.
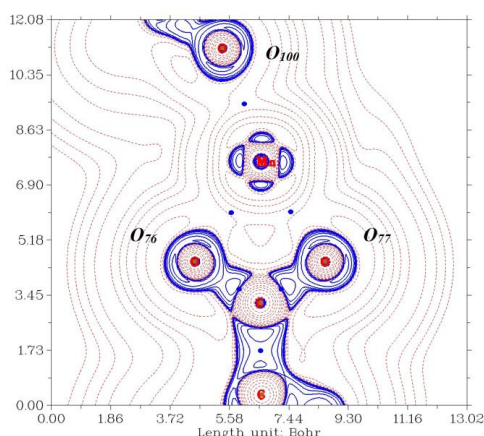
Moreover, the values of $|V(r_b)|/G(r_b)$ are more significant than one for all three BCPs, indicating that they are interactions of an intermediate character between electrostatic and covalent bonds (polarized coordinated bonds), which is in agreement with the ELF analysis. Furthermore, the electronic charge density values indicate that these bonds are the weakest. Considering that the values of second-order hyperconjugative energies for the O_{76}-Zn and O_{77}-Zn interactions were the lowest obtained, it is suggested that the electrostatic component is more accentuated in this system, since the resonance effect would be less

Figure 18. Contour map of $\nabla^2 \rho$ of ALG-Zn-GO. The solid and dashed lines correspond to the negative regions and positive regions of $\nabla^2 \rho$, respectively. The blue dots correspond to critical binding points.

Table 11. Local topological properties at the critical binding points in the ALG-Zn-GO system.

ALG-Zn-GO	O_{100}-Zn	O_{76}-Zn	O_{77}-Zn
$\nabla^2 \rho_{BCP}$ (a.u.)	0,4789	0,4475	0,3971
ρ_{BCP} (a.u.)	0,0740	0,0780	0,0720
$G(r_b)$ (a.u.)	0,0983	0,0955	0,0866
$V(r_b)$ (a.u.)	-0,1027	-0,1041	-0,0953
L_{r_b} (a.u.)	-0,0938	-0,0869	-0,0779
$H(r_b)$ (a.u.)	-0,0045	-0,0086	-0,0087
$|V(r_b)|/G(r_b)$	1,0453	1,0904	1,1007

4.3.4. ALG-Mn-GO

Figure 19 shows the Laplacian diagram of the electron density for ALG-Mn-GO. In this diagram, an intense polarization of the valence layer of the Mn atom is observed, where there is charge leakage in the direction of the BCP (3, -1) of the interactions with the three oxygen atoms. The three oxygen atoms are polarized, where O_{76} and O_{77} show a slight charge leakage towards the metal. The charge concentration of the lone pairs on O_{100} is less distorted. These results are consistent with the ELF analysis, where charge transfer from the metal to the oxygen is the significant contribution to this interaction.

Table 12 summarizes the values of the local properties of the three BCPs. The values of $\nabla^2 \rho_{BCP}$ are positive, which indicates that they are closed-layer interactions. The values of the electronic charge density follow the trend of the previous systems (except for the one where the bridge metal is Zn), in which the lowest values for this magnitude were obtained. Meanwhile, the values of $L_{(r_b)}$ and $H_{(r_b)}$ are less than zero. As already mentioned, in these cases, the opposite trend between $H_{(r_b)}$ and ρ_{BCP} tells us that the electrostatic component is the one that stabilizes the system.

Finally, the interval for the ratio of the absolute value of the potential energy density concerning the kinetic energy density is more significant than one, which reveals the intermediate character of the electrostatic and covalent components of the bonds formed. These results are consistent with the ELF results. According to the second-order hyperconjugative energy values obtained in the NBO study, there is a high charge delocalization in this system, so the electronic resonance effect is important in the structural stabilization of this system.

Figure 19. Contour map of $\nabla^2 \rho$ of ALG-Mn-GO. The solid and dashed lines correspond to the negative regions and positive regions of $\nabla^2 \rho$, respectively. Blue dots correspond to critical binding points.

Table 12. Local topological properties at critical junction points in the ALG-Mn-GO system.

ALG-Mn-GO	O_{100}-Mn	O_{76}-Mn	O_{77}-Mn
$\nabla^2 \rho_{BCP}$ (a.u.)	0,5005	0,4521	0,4826
ρ_{BCP} (a.u.)	0,0770	0,0840	0,0800
$G(r_b)$ (a.u.)	0,1310	0,1232	0,1322
$V(r_b)$ (a.u.)	-0,1369	-0,1334	-0,1438
L_{r_b} (a.u.)	-0,1251	-0,1130	-0,1206
$H(r_b)$ (a.u.)	-0,0059	-0,0102	-0,0116
$|V(r_b)|/G(r_b)$	1,0452	1,0829	1,0875

Finally, the NBO, ELF, and QTAIM analysis revealed interactions of a coordinated nature, where the electrostatic component is important. The high electronic delocalization, a product of the oxygen-metal interactions, generates high electronic delocalization so that the mesomeric effect would influence the stabilization of the systems under study. These results show that the systems with the most substantial interactions were ALG-Co-GO, followed by ALG-Cu-GO. However, the latter does not generate an important interaction with O_{77}, and the former presented a higher degree of electronic delocalization. Then the ALG-Mn-GO system presented slightly weaker bonds with the three oxygens, according to the electronic charge density values of the QTAIM analysis, with a high electronic delocalization. Finally, the ALG-Zn-GO system presented the weakest bonds, where the electrostatic component would be important in stabilizing the system. The characteristics of the interactions formed could be attributed to the presence of d orbitals in the studied metals, which can accept the charge in their empty orbitals (67).

Previous experimental studies have shown that the ALG-GO mixture has a high degree of adsorption for Cu^{2+} and Co^{2+} which has been related to the affinity of this mixture for these metals (21; 68). All of the above would agree with the type of interactions reported in this study. Likewise, this mixture presents a high degree of adsorption for Mn^{2+} and Zn^{2+} (69; 70). However, the high amount of -OH, -O- and -COO- groups present in the hydrocarbon skeleton of alginate would be the main responsible for these results (4; 71). The same studies show that the physical adsorption phenomenon is important (18; 72), so forming coordinated bonds would be one of many factors influencing the adsorption process. The type of interaction studied in this work is important in the adsorption phenomenon and the morphology of the resulting structure. For example, previous studies show that after the desorption process, the ALG-Co-GO beads tend to maintain a structure similar to the original (73), while the beads of the ALG-Zn-GO system present a bulky and agglomerated morphology (69). The morphology would be related to the type of adsorbed metal due to a crosslinking process (12). Other studies report that the morphological characteristics after the desorption process of ALG-Mn-GO remain almost unchanged concerning the original ones (70). Also, it has been proved that after the desorption of Cu^{2+} ion, the porous structure formed by intertwined fibers mitigates the volume change during the adsorption process, where the reusability of the material is only reduced by 3% (68). Studies on the morphology generated in the ALG-GO mixture, using the metals Ca^{2+}, Ba^{2+}, and Fe^{3+}, showed that the most stable structure with better physical properties was the one generated with Fe^{3+} (74). The latter presents 3d orbitals available, allowing it to form bonds with similar characteristics to those reported in this study. Thus, the type of interaction generated in the bonding of alginate and graphene oxide, through the carboxylic groups present in both substances, could be fundamental in the adsorption capacity of the different metals under study due to its influence on the type of morphology of the adsorbent system.

CONCLUSIONS

The results obtained through the different theoretical models used in this study showed that the metals Co^{2+}, Cu^{2+}, Mn^{2+}, and Zn^{2+} form coordinated type bonds with a high electrostatic component, which varies according to the metal, with the carboxylic groups of alginate and graphene oxide, acting as a bridge between both substances. According to the degree of electronic delocalization, the binding strength and stability order of the systems under study were as follows; ALG-Cu-GO > ALG-Co-GO > ALG-Mn-GO > ALG-Zn-GO. These results are shown to be correlated with adsorption capacity results for the alginate-graphene oxide mixture.

REFERENCES

1. Yaashikaa P, Kumar PS, Karishma SJER. (2022). Review on biopolymers and composites–Evolving material as adsorbents in removal of environmental pollutants. *Environ. Res.*212:113114
2. Rhimi A, Zlaoui K, Horchani-Naifer K, Ennigrou DJJIPJ. (2022). Characterization and extraction of sodium alginate from Tunisian algae: synthesizing a cross-linked ultrafiltration membrane. *Iran. Polym.* J.31:367-82
3. Shaikh MAJ, Alharbi KS, Almalki WH, Imam SS, Albratty M, et al. (2022). Sodium alginate based drug delivery in management of breast cancer. *Carbohydr. Polym.*119689
4. Gao X, Guo C, Hao J, Zhao Z, Long H, Li MJIjobm. (2020). Adsorption of heavy metal ions by sodium alginate based adsorbent-a review and new perspectives. *Int. J. Biol. Macromol.* 164:4423-34.
5. Sanchez-Ballester NM, Bataille B, Soulairol IJCP. (2021). Sodium alginate and alginic acid as pharmaceutical excipients for tablet formulation: Structure-function relationship. *Carbohydr. Polym.* 270:118399.
6. Martinsen A, Skjåk-Bræk G, Smidsrød OJB, bioengineering. (1989). Alginate as immobilization material: I. Correlation between chemical and physical properties of alginate gel beads. *Biotechnol. Bioeng.*33:79-89.
7. Johnson FA, Craig DQ, Mercer ADJJop, pharmacology. (1997). Characterization of the block structure and molecular weight of sodium alginates. *J. Pharm. Pharmacol.* 49:639-43.
8. Fu S, Thacker A, Sperger DM, Boni RL, Buckner IS, et al. (2011). Relevance of rheological properties of sodium alginate in solution to calcium alginate gel properties. *AAPS PharmSciTech.* 12:453-60
9. Ngah WW, Fatinathan SJCEJ. (2008). Adsorption of Cu (II) ions in aqueous solution using chitosan beads, chitosan–GLA beads and chitosan–alginate beads. *Chem. Eng. J.* 143:62-72
10. Gokila S, Gomathi T, Sudha P, Anil SJIjobm. (2017). Removal of the heavy metal ion chromiuim (VI) using Chitosan and Alginate nanocomposites. *Int. J. Biol. Macromol.* 104:1459-68.
11. Yadav M, Rhee KY, Park SJCp. (2014). Synthesis and characterization of graphene oxide/carboxymethylcellulose/alginate composite blend films. *Carbohydr. Polym.*110:18-25
12. Serrano-Aroca Á, Ruiz-Pividal J-F, Llorens-Gámez MJSr. (2017). Enhancement of water diffusion and compression performance of crosslinked alginate films with a minuscule amount of graphene oxide. *Sci. Rep.*7:1-8
13. Ionita M, Pandele MA, Iovu HJCp. (2013). Sodium alginate/graphene oxide composite films with enhanced thermal and mechanical properties. *Carbohydr. Polym.* 94:339-44
14. Suk JW, Piner RD, An J, Ruoff RSJAn. (2010). Mechanical properties of monolayer graphene oxide. *ACS Nano.* 4:6557-64
15. Zhu Y, Murali S, Cai W, Li X, Suk JW, et al. (2010). Graphene and graphene oxide: synthesis, properties, and applications. *Adv. Mater.*22:3906-24

16. Brisebois P, Siaj MJJoMCC. (2020). Harvesting graphene oxide–years 1859 to 2019: a review of its structure, synthesis, properties and exfoliation. *J. Mater. Chem. C* 8:1517-47

17. Li J, Ma J, Chen S, Huang Y, He JJMS, C E. (2018). Adsorption of lysozyme by alginate/graphene oxide composite beads with enhanced stability and mechanical property. *Mater. Sci. Eng.* 89:25-32

18. Ji C, Yang S, Tao E, Cheng Y, Hao X, Li YJJoECE. (2021). Three-dimensional network graphene oxide/sodium alginate aerogel beads with slit-shaped structure: Synthesis, performance and selective adsorption mechanism for Cu (II). *J. Environ. Chem.* Eng.9:106819

19. Serrano-Aroca Á, Iskandar L, Deb SJEPJ. (2018). Green synthetic routes to alginate-graphene oxide composite hydrogels with enhanced physical properties for bioengineering applications. *Eur. Polym. J.*103:198-206

20. Sabater i Serra R, Molina-Mateo J, Torregrosa-Cabanilles C, Andrio-Balado A, Meseguer Dueñas JM, Serrano-Aroca ÁJP. (2020). Bio-nanocomposite hydrogel based on zinc alginate/graphene oxide: Morphology, structural conformation, thermal behavior/degradation, and dielectric properties. *Polym.*12:702

21. Algothmi WM, Bandaru NM, Yu Y, Shapter JG, Ellis AVJJoc, science i. (2013). Alginate–graphene oxide hybrid gel beads: An efficient copper adsorbent material. *J. Colloid Interface Sci.*397:32-8

22. Weinhold F, Landis C, Glendening EJIRiPC. (2016). What is NBO analysis and how is it useful? *Int. Rev. Phys. Chem.*35:399-440

23. Lin X, Wu W, Mo YJCCR. (2020). A theoretical perspective of the agostic effect in early transition metal compounds. *Coord. Chem. Rev.* 419:213401

24. Platts JA, Baker RJJDT. (2020). A computational investigation of orbital overlap versus energy degeneracy covalency in [UE 2] 2+(E= O, S, Se, Te) complexes. *Dalton Trans.* 49:1077-88

25. Liu S, Rong C, Lu T, Hu HJTJoPCA. (2018). Identifying strong covalent interactions with Pauli energy. *J. Phys. Chem.*122:3087-95

26. Fuentealba P, Chamorro E, Santos JC. (2007). Understanding and using the electron localization function. *Theor. Comput. Chem.*19:57-85

27. Savin A, Becke A, Flad J, Nesper R, Preuss H, Von Schnering HJACIEiE. (1991). A new look at electron localization. *Angew. Chem.* 30:409-12

28. Savin A, Nesper R, Wengert S, Fässler TFJACIEiE. (1997). ELF: The electron localization function. *Angew. Chem.* 36:1808-32

29. Chauvin R, Lepetit C, Silvi B, Alikhani E. (2016). *Applications of topological methods in molecular chemistry*. Springer

30. Rodríguez JIJJocc. (2013). An efficient method for computing the QTAIM topology of a scalar field: The electron density case. *J. Comput. Chem.* 34:681-6

31. Popelier PLA, Aicken F, O'Brien S. (2000). *Atoms in molecules*. Prentice Hall Manchester

32. Malcolm NO, Popelier PLJFd. (2003). The full topology of the Laplacian of the electron density: scrutinising a physical basis for the VSEPR model. *Faraday Discuss.*124:353-63

33. Popelier PJCCR. (2000). On the full topology of the Laplacian of the electron density. *Coord. Chem. Rev.* 197:169-89

34. Wang J-J, Chen X, Zhang B-S, Li C-B, Wang Y-FJJoMS. (2021). Experimental (X-ray, TGA) and computation (NBO, AIM) studies of Iron (II) complex with thiabendazole and 5-aminoisophthalate. *J. Mol. Struct.*1245:131100

35. Lu X, Duchimaza-Heredia J, Cui QJTJoPCA. (2019). Analysis of Density Functional Tight Binding with Natural Bonding Orbitals. *J. Phys. Chem* 123:7439-53

36. Lee LP, Cole DJ, Payne MC, Skylaris CKJJocc. (2013). Natural bond orbital analysis in the ONETEP code: applications to large protein systems. *J. Comput. Chem.*34:429-44

37. Vektarienė AJLJoP. (2018). The transition metal to ligand bonding nature: a quantum chemical study of π-allyl-ruthenacycle molecule. *Lith. J. Phys.*58

38. Karafiloglou PJJoCC. (2001). A method to calculate the weights of nbo electronic structures from Moffitt's theorem. *J. Comput. Chem.* 22:306-15

39. Zülfikaroğlu A, Batı H, Dege NJJoMS. (2018). A theoretical and experimental study on isonitrosoacetophenone nicotinoyl hydrazone: Crystal structure, spectroscopic properties, NBO, NPA and NLMO analyses and the investigation of interaction with some transition metals. *J. Mol. Struct.*1162:125-39

40. Tsirelson V, Stash AJCpl. (2002). Determination of the electron localization function from electron density. *Chem. Phys. Lett.* 351:142-8

41. Nalewajski RF, Köster AM, Escalante SJTJoPCA. (2005). Electron localization function as information measure. *J. Phys. Chem. A* 109:10038-43

42. Kohout M, Wagner FR, Grin YJTCA. (2002). Electron localization function for transition-metal compounds. *Theor Chem Acc* 108:150-6

43. Zou G, Jo H, Lim SJ, You TS, Ok KMJACIE. (2018). Rb3VO (O2) 2CO3: a four-in-one carbonatoperoxovanadate exhibiting an extremely strong second-harmonic generation response. *Angew. Chem.* 57:8619-22

44. Jerabek P, Schuetrumpf B, Schwerdtfeger P, Nazarewicz WJPRL. (2018). Electron and nucleon localization functions of oganesson: approaching the thomas-fermi limit. Phys. Rev. Lett. 120:053001

45. Mierzwa G, Gordon AJ, Berski SJJoMS. (2020). The nature of the triple BB, double, BB, single, B–B, and one-electron, BB boron-boron bonds from the topological analysis of electron localization function (ELF) perspective. *J. Mol. Struct.*1221:128530.

46. Fuster F, Dézarnaud-Dandine C, Chevreau H, Sevin AJPCCP. (2004). A theoretical study of the bonding in NO,(NO) 2,(NO) 2− and (NO) 2 2−using a topological analysis of the electron localization function. *Phys. Chem. Chem. Phys.* 6:3228-34.

47. Pilme J, Silvi B, Alikhani MEJTJoPCA. (2003). Structure and stability of M− CO, M= first transition-row metal: An application of density functional theory and topological approaches. *J. Phys.Chem. A* 107:4506-14.

48. Durlak P, Latajka Z, Berski SJTJocp. (2009). A Car–Parrinello and path integral molecular dynamics study of the intramolecular lithium bond in the lithium 2-pyridyl-N-oxide acetate. *J. Phys.Chem.* 131:024308

49. Pendás AM, Francisco E, Blanco MJCPL. (2008). Electron–electron interactions between ELF basins. *Chem. Phys. Lett*. 454:396-403

50. Savin A, Silvi B, Colonna FJcjoc. (1996). Topological analysis of the electron localization function applied to delocalized bonds. *Can. J. Chem.* 74:1088-96

51. Mierzwa G, Gordon AJ, Berski SJNJoC. (2018). On the nature of the boron–copper interaction. Topological study of the electron localisation function (ELF). *New J. Chem.* 42:17096-114

52. Koumpouras K, Larsson JAJJoPCM. (2020). Distinguishing between chemical bonding and physical binding using electron localization function (ELF). *J. Phys.: Condens. Matter* 32:315502

53. Lepetit C, Kahn MLJRoCI. (2021). QTAIM and ELF topological analyses of zinc-amido complexes. *Res. Chem. Intermed*. 47:377-95

54. Mierzwicki K, Berski S, Latajka ZJCPL. (2000). Nature of chemical bonds in MCCH (M= Li, Na, K) based on the topological analysis of electron localisation function (ELF) and electron density. *Chem. Phys. Lett.* 331:538-46

55. Gassoumi B, Mehri A, Hammami H, Castro M, Karayel A, et al. (2022). Spectroscopic characterization, host-guest charge transfer, Hirshfeld surfaces, AIM-RDG and ELF study of adsorption and chemical sensing of heavy metals with new derivative of Calix [4] quinone: A DFT-D3 computation. *Mater. Chem. Phys.* 278:125555

56. Michalski M, Gordon AJ, Berski SJP. (2021). Theoretical insights and quantitative prediction of the nature of boron–chalcogen (O, S, Se, Te) interactions using the electron density and the electron localisation function (ELF). *Polyhedron*. 210:115495

57. Poater J, Duran M, Sola M, Silvi BJCr. (2005). Theoretical evaluation of electron delocalization in aromatic molecules by means of atoms in molecules (AIM) and electron localization function (ELF) topological approaches. *Chem. Rev.* 105:3911-47

58. Lu T, Chen FJTJoPCA. (2013). Bond order analysis based on the Laplacian of electron density in fuzzy overlap space. *J. Phys. Chem. A*. 117:3100-8

59. Korabel'nikov DV, Zhuravlev YNJRa. (2019). The nature of the chemical bond in oxyanionic crystals based on QTAIM topological analysis of electron densities. *RSC Adv.* 9:12020-33

60. Cukrowski I, Govender KK, Mitoraj MP, Srebro MJTJoPCA. (2011). QTAIM and ETS-NOCV analyses of intramolecular CH··· HC interactions in metal complexes. *J. Phys. Chem. A* 115:12746-57

61. Kazachenko AS, Akman F, Abdelmoulahi H, Issaoui N, Malyar YN, et al. (2021). Intermolecular hydrogen bonds interactions in water clusters of ammonium sulfamate: FTIR, X-ray diffraction, AIM, DFT, RDG, ELF, NBO analysis. *J. Mol. Liq.* 342:117475

62. Louit G, Hocquet A, Ghomi M, Meyer M, Sühnel JJP. (2003). Guanine tetrads interacting with metal ions. An AIM topological analysis of the electronic density. *PhysChemComm.* 6:1-5

63. Arnold WD, Oldfield EJJotACS. (2000). The chemical nature of hydrogen bonding in proteins via NMR: J-couplings, chemical shifts, and AIM theory. *J. Am. Chem. Soc.* 122:12835-41

64. Cukrowski I, de Lange JH, Mitoraj MJTJoPCA. (2014). Physical nature of interactions in ZnII complexes with 2, 2′-bipyridyl: Quantum theory of atoms in molecules (QTAIM), interacting quantum atoms (IQA), noncovalent interactions (NCI), and extended transition state coupled with natural orbitals for chemical valence (ETS-NOCV) comparative studies. *J. Phys. Chem. A* 118:623-37

65. Li L, Wu C, Wang Z, Zhao L, Li Z, et al. (2015). Density functional theory (DFT) and natural bond orbital (NBO) study of vibrational spectra and intramolecular hydrogen bond interaction of l-ornithine–l-aspartate. *Spectrochim. Acta, Part A*. 136:338-46

66. Glendening ED, Landis CR, Weinhold FJWircms. (2012). Natural bond orbital methods. *Wiley Interdiscip. Rev.: Comput. Mol. Sci.* 2:1-42

67. Zhou Y, Pan S, Dong X, Wang L, Zhou M, Frenking GJJotACS. (2022). Generation and Characterization of the Charge-Transferred Diradical Complex CaCO2 with an Open-Shell Singlet Ground State. *J. Am. Chem. Soc.* 144, 18, 8355–8361

68. Pan L, Wang Z, Yang Q, Huang RJN. (2018). Efficient removal of lead, copper and cadmium ions from water by a porous calcium alginate/graphene oxide composite aerogel. *Nanomaterials.* 8:957

69. Abd-Elhamid A, Elgoud E, Aly HJC. (2022). Alginate modified graphene oxide for rapid and effective sorption of some heavy metal ions from an aqueous solution. *Cellulose*. 1-15

70. Yang X, Zhou T, Ren B, Hursthouse A, Zhang YJSr. (2018). Removal of Mn (II) by sodium alginate/graphene oxide composite double-network hydrogel beads from aqueous solutions. *Sci. Rep*. 8:1-16

71. Bai C, Wang L, Zhu ZJIjobm. (2020). Adsorption of Cr (III) and Pb (II) by graphene oxide/alginate hydrogel membrane: Characterization, adsorption kinetics, isotherm and thermodynamics studies. *Int. J. Biol. Macromol*. 147:898-910

72. Priya VN, Rajkumar M, Mobika J, Sibi SLJPEL-dS, Nanostructures. (2021). Alginate coated layered double hydroxide/reduced graphene oxide nanocomposites for removal of toxic As (V) from wastewater. *Phys. E (Amsterdam, Neth.)*. 127:114527

73. Sun Y, Li Y, Chen B, Cui M, Xu W, et al. (2022). High-Efficiency Adsorption Performance of Cobalt Alginate/Graphene Oxide Aerogel Prepared by Green Method for Methylene Blue. *ChemistrySelect.* 7:e202201216

74. Zheng H, Yang J, Han SJJoAPS. (2016). The synthesis and characteristics of sodium alginate/graphene oxide composite films crosslinked with multivalent cations. *J. Appl. Polym. Sci.*133